buildings

MDPI

Article

Study on Spatial Effects of Non-Symmetric Cable-Stayed Bridges Under Operational Loads

Xiaogang Li [1,*], Qin Wang [1], Peng Ding [2], Minglin Zhou [1], Xiaohu Chen [2] and Shanxing Xiang [1]

[1] School of Civil and Hydraulic Engineering, Chongqing University of Science and Technology, Chongqing 401331, China; 2023206039@cqust.edu.cn (Q.W.); 2023206097@cqust.edu.cn (M.Z.); 2025207036@cqust.edu.cn (S.X.)

[2] T. Y. Lin International Engineering Consulting (China) Co., Ltd., Chongqing 401121, China; dingpeng@tylin.com.cn (P.D.); chenxiaohu@tylin.com.cn (X.C.)

* Correspondence: 2021058@cqust.edu.cn

Abstract

Addressing the issues of the complex mechanical responses and significant spatial effects of asymmetric large-span cable-stayed steel box girder bridges with shared public-rail traffic under operational loads (live load, static wind, and structural temperature differences), this paper uses the Lijiatuo Yangtze River Double-Line Bridge on Chongqing Metro Line 18 as the engineering background to construct multi-scale finite element models for the entire bridge and the closure segment, and validates them against GNSS displacement and strain monitoring data from the actual bridge. The study shows that the spatiotemporal asymmetry of operational live loads induces significant lateral bias effects in the main bridge, resulting in reverse displacements in the mid-span section, and with stress distributions characterized by "oscillation in the side spans and concentration in the mid-span." The study also shows that, under static wind loads, the bridge's lateral displacement approximately increases linearly with wind speed, and the mid-span response is higher than that of the side spans, showing significant spatial sensitivity to wind loads. Finally, the study shows that, although the system temperature difference causes small overall displacements, it still induces symmetrical lateral deformations and local stress concentrations near the closure segment. Local refined analyses further reveal the displacement distribution mechanism of the closure segment under operational loads. The health monitoring data agree well with the simulation results, validating the reliability of the numerical model. The research systematically reveals the spatial mechanical behavior of such bridges under operational loads, providing theoretical basis and engineering references for the design optimization and safety monitoring of similar asymmetric cable-stayed bridges.

Keywords: the asymmetric cable-stayed bridge with the same level of road and rail; large-span steel box girder; spatial effect; live load effect; static wind load; system temperature difference

Academic Editor: Giuseppina Uva

Received: 16 December 2025
Revised: 23 January 2026
Accepted: 13 February 2026
Published: 17 February 2026

1. Introduction

To address the current situation of increasing traffic volume and scarce bridge resources, the monorail and road dual-purpose bridge has been actively utilized due to its advantages of integrated transportation and higher carrying capacity. Compared with conventional symmetrically arranged cable-stayed bridges, the large-span steel box girder cable-stayed bridge with asymmetric layout on the same level of the road and railway has the lane and track area located on both sides of the main girder in space, and the stiffness

center and load action center do not coincide. In terms of time, railway trains operate at night while road traffic runs almost 24/7, causing the structure to be in a state of partial loading for a long time. At the same time, its sensitivity to wind loads and temperature loads has also significantly increased. Therefore, it is very necessary to study the lateral effect of a large-span steel box girder cable-stayed bridge with asymmetric layout on the same level as a road and railway.

At present, scholars both at home and abroad have conducted certain research on the lateral effects of bridges. Among these, Man Zhou et al. [1] explored the lateral mechanical effects of box girder prefabricated segments with CSW under vehicle loads in elastic and cracked states. Li Gang et al. [2] studied the mechanical characteristics and live load effects of ultra-wide steel box girders in road–rail level deck cable-stayed bridges. Liu Anshuang and Li Xiaogang et al. [3] proposed reasonable value suggestions for large-span track suspension bridges based on existing domestic and international bridge codes, and verified the rationality of the suggested limit range for large-span track suspension bridges through static characteristics and wind–vehicle–bridge coupling vibration analysis. Zhang Pengfei and Wen Yue et al. [4] established a finite element model to analyze the lateral mechanical effects of the track structure on a bridge under transverse wind loads. Li Shengyang et al. [5] focused on the lateral mechanical effects of A-shaped bridge towers without lower crossbeams under static loads. Mutashar et al. [6] discussed the mechanical effects of typical skew composite adjacent box girder bridges under live loads. Chen Yuwei et al. [7], based on the heat conduction theory and ABAQUS finite element numerical simulation, analyzed the temperature difference and temperature stress distribution characteristics of the steel–concrete composite section of wide-span hybrid girder cable-stayed bridges under non-uniform solar radiation. Deng Wenqin and Zhang Wenjin et al. [8] studied the influence of different cross-sectional forms of steel–concrete composite girder bridge decks on the lateral bending effect. Hu Hao and Gao Ce et al. [9] analyzed the local mechanical behavior of the main girder of large-span railway single-plane prestressed concrete low-tower cable-stayed bridges. Zhao H and Ding Y et al. [10], based on the use of a wavelet transform to separate temperature-induced and vehicle-induced deflections, verified the deflection's sensitivity to temperature, analyzed the influence of temperature-induced deformation on vehicle-induced deflection, and described the statistical laws of vehicle-induced deflection. Crespi P and Zucca M et al. [11] proposed a multi-modal pushover efficient evaluation program, which can take into account the nonlinear mechanical behavior and complex dynamic response characteristics of reinforced concrete bridges under the premise of controlling the computational load.

In conclusion, existing research has largely focused on conventional symmetrical bridges, and there is still a lack of systematic study on the lateral effects of such long-span, same-level, asymmetric steel box girder cable-stayed bridges for combined road–rail use. Given that their lateral effects are particularly sensitive to wind loads and the spatial and temporal asymmetry of live loads is pronounced, this paper takes China's first bridge of this type—the Lijiatuo Yangtze River Double-Line Bridge on Chongqing Rail Transit Line 18—as the background. Using MIDAS/Civil and MIDAS FEA NX (2022 v1.1) software, full-bridge and localized refined finite element models were established, with lateral displacement and stress as the main indicators. The loads experienced by the structure during service, including road and rail transit live loads, wind loads, and temperature loads, are collectively referred to as operational loads. The study aims to reveal the lateral mechanical behavior and structural response mechanisms under operational loads, providing theoretical support for the design, construction, and health monitoring of similar bridges, and serving as a reference for enhancing the safety and durability of long-span bridges under complex loading conditions.

2. Related Structural Theory

(1) Influence of Asymmetric Arrangement on Lateral Mechanical Behavior

For the cross-section of the main beam of the bridge, the stiffness center can be approximately regarded as the weighted center of the flexural stiffness (EI) of each component. In the cross-section of this bridge, there are differences in the structural form and stiffener arrangement between the lane area and the rail travel area, resulting in a lateral bending stiffness of the EI_y that is not symmetrical about the centerline, a center of stiffness that is $C_k(x_k, y_k)$, and a resulting action point of the vehicle live load that becomes $C_p(x_p, y_p)$. In an asymmetrical arrangement $x_k \neq x_p$. When the load-resultant action line does not pass through the stiffness center, the main beam not only undergoes lateral bending, but also produces torsion around the vertical axis (z-axis), and its differential relationship can be expressed as follows [12,13]:

$$\begin{cases} EI_y \frac{d^4 v(x)}{dx^4} = q_y(x) \\ EI_\omega \frac{d^4 \varnothing(x)}{dx^4} - GI_t \frac{d^2 \varnothing(x)}{dx^2} = m_z(x) \end{cases} \quad (1)$$

In the formula, $v(x)$ is the lateral displacement of the bridge; $\varnothing(x)$ is the torsion angle; EI_y is the section's lateral bending stiffness; EI_ω is the section's constrained torsional stiffness; GI_t is the section's free torsional stiffness; $q_y(x)$ is the lateral distributed load; $m_z(x) = q_y(x) * e$ is the distributed torque; and e = $x_p - x_k$ is the load eccentricity.

(2) Shear hysteresis effect

For asymmetrical wide steel box girders, the shear lag effect significantly exacerbates the non-uniform distribution of transverse stresses in the cross-section. When the load is eccentric, the flange on the side away from the load (top and bottom plates) cannot fully develop its compressive capacity, resulting in stress concentration in the flange on the side near the load. Longitudinal normal stress considering the shear lag effect $\sigma_x(y, z)$ can be corrected to the following:

$$\sigma_x(y, z) = \frac{M_y Z}{I_y}[1 + \psi(y)] \quad (2)$$

In the formula, M_y represents the lateral bending moment; I_y represents the lateral moment of inertia; and $\psi(y)$ is a stress distribution function describing the shear hysteresis effect, and its value is related to the cross-sectional shape, load position, and boundary conditions.

Among these, the transverse bending moment, torsion, and shear force lag in such beams are coupled into the same mechanism: uneven loading simultaneously generates a transverse bending moment and distributed torque. The web shear flow not only transmits the transverse shear force but also superimposes the torsional shear flow. The flange shear flow spreads out, causing the longitudinal normal stress to be non-linearly distributed laterally. The magnitude of $\psi(y)$ is determined by the transverse shear force, torque and support conditions. Additionally, after the effective flange width is compressed by the shear lag, the bending/torsion stiffness of the section decreases, which in turn amplifies the transverse deflection and torsional angle. Therefore, the subsequent analysis adopts the "full bridge + local" approach, which is based on the above coupling understanding.

(3) Live Load Impact Factor

The live load impact factor is a design factor that equates the dynamic effects of moving loads to amplified static effects, as follows [14]:

When L $\leq$ 50 m, we find the following:

$$\mu = \frac{0.15}{1 + 0.5L} \tag{3}$$

When L > 50 m, we find the following:

$$\mu = 0.05 \tag{4}$$

(4) Equivalent Static Wind Load

According to the "Code for Wind-Resistant Design of Highway Bridges" [15], the basic wind speed for bridge design is as follows:

$$U_{S10} = (K_c - U_{10}) \tag{5}$$

In the formula, U_{S10} is the basic wind speed under standard site conditions at a height of 10 m, K_c is the site category conversion coefficient for wind speed, and U_{10} is the maximum wind speed with a return period of several years at an observation station or a design location 10 m high under non-standard site conditions.

Design reference wind speed at the reference height Z of the bridge or component U_d is as follows:

$$U_d = K_f \frac{(Z)}{10}^{\alpha_0} U_{S10} \tag{6}$$

In the formula, U_d is the design reference wind speed, K_f is the wind resistance risk factor, Z is the reference height of the bridge or component, and α_0 is the surface roughness coefficient at the bridge site.

Equivalent gust wind speed U_g (m/s) is as follows:

$$U_g = G_v U_d \tag{7}$$

In the formula, G_v is the equivalent static gust factor.

Equivalent static gust load in the downwind direction per unit length of the main beam under wind action on the transverse bridge F_g is as follows:

$$F_g = \frac{1}{2}\rho {U_g}^2 C_H D \tag{8}$$

In the formula, ρ is the air density, C_H is the transverse force coefficient of the main beam, and D is the characteristic height of the main beam.

(5) System Temperature Difference

According to the "Code for Design of Urban Rail Transit Bridges" [14], the system temperature difference should be calculated starting from the time of structural closure, and it is recommended to take the difference between the closure temperature and the historical extreme minimum and maximum temperatures separately.

$$\begin{cases} \Delta T_1 = T_{H_1} - T_{L_1} \\ \Delta T_2 = T_{H_2} - T_{L_2} \end{cases} \tag{9}$$

In the formula, ΔT_1 and ΔT_2 are the overall temperature rise differences, respectively; T_{H_1} and T_{H_2} are the record highest annual temperature and the highest temperature at the time of closure, respectively; and T_{L_1} and T_{L_2} are the lowest temperature at the time of closure and the record lowest temperature, respectively.

3. Project Overview

The Li Jia Tou Yangtze River Duplex Bridge project starts from the Qionglong Peninsula in Jiulongpo District and ends at Li Jia Tou in Bapan District. The duplex bridge is located approximately 52 m upstream of the current Li Jia Tou Yangtze River Bridge and crosses the Yangtze River in parallel. The total length of the bridge is 1306.2 m. The main bridge is a (68.4 + 150.8 + 454 + 161.3 + 102.2 + 50) m double-tower double-cable surface six-span steel box girder dual-track and dual-rail dual-purpose cable-stayed bridge. The bridge deck is designed to be non-symmetrically arranged on the same level for both public and railway use. P1, P4, and P5 are auxiliary piers, and P6 is the connection pier. The layout of the main bridge is shown in Figure 1. The upstream side is a municipal road (the Fourth Vertical Line) with a single lane in each direction, and the downstream side is a double-track rail transit (Line 18). The main beam is a monolithic steel box girder, with a beam height of 4.0 m at the centerline and a total width of 33.95 m. The cross-sectional layout is as follows: 1.025 (wind nozzle) + 2.2 m (inspection cable zone) + 15.5 m (traffic lane) + 0.4 (anti-collision guardrail) + 1.2 m (anti-collision isolation zone) + 10.4 m (railway area) + 2.2 m (inspection lane and cable zone) + 1.025 (wind nozzle) = 33.95 m. The cross-sectional layout of the main beam is shown in Figure 2. The bridge towers are diamond-shaped H-type bridge towers. The top elevation of the P2 and P3 bridge towers is 342.0 m, and a 3.0-meter-high tower base is set. The total height of the P2 bridge tower is 179.5 m, with a bottom elevation of 162.5 m, and the total height of the P3 bridge tower is 174.5 m, with a bottom elevation of 167.5 m. P2 and P3 bridge towers are composed of three tower columns in the upper, middle, and lower sections and two cross beams. The upper and lower tower columns are hollow thin-walled sections, and the lower tower column and lower cross beam adopt hollow sections. Except for the anti-collision filling concrete of the lower tower column's anti-collision part, which uses C25, the rest are all C50 concrete. The upper and lower tower columns (without cable zone) and the main tower are of ordinary reinforced concrete structure. The upper and lower cross beams of the bridge towers are of prestressed concrete structure. The cross-sectional view of the bridge towers is shown in Figure 3. The anchorage of the cable stays is set at the tower ends as tensioning ends, and the ends of the beam are anchoring ends. P2 and P3 tower sides are respectively equipped with 40 pairs of cable stays, using Φ7.0 mm zinc–aluminum alloy high-strength low-relaxation parallel steel wire HDPE-sheathed finished cables, with tensile strength not less than 1670 MPa. The cable stay numbers are as follows: the side span and main span of the Qionglong side are NA20 to NA01, NJ01 to NJ20, and the side span and main span of the Bapan side are SA20 to SA01, SJ01 to SJ20. A cross-sectional view of the cable stays is shown in Figure 4.

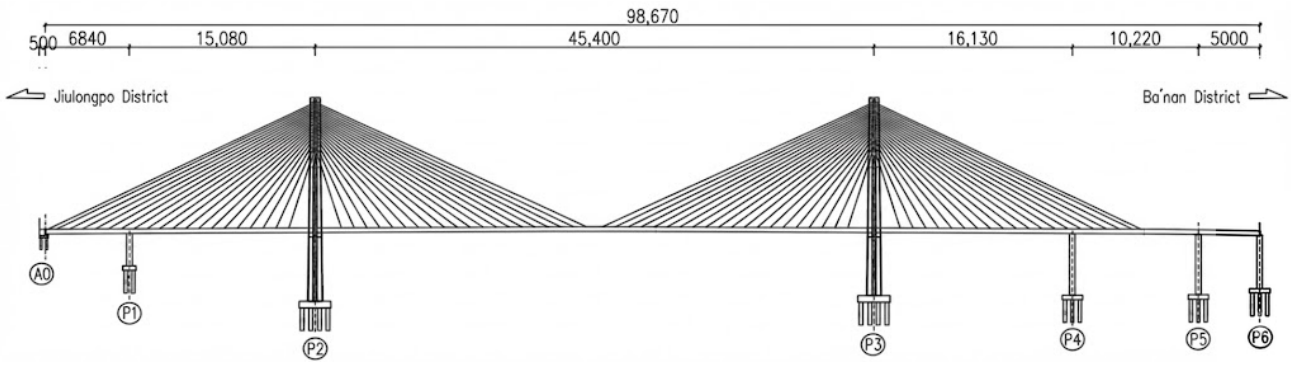

Figure 1. Layout of the main bridge structure (unit: cm).

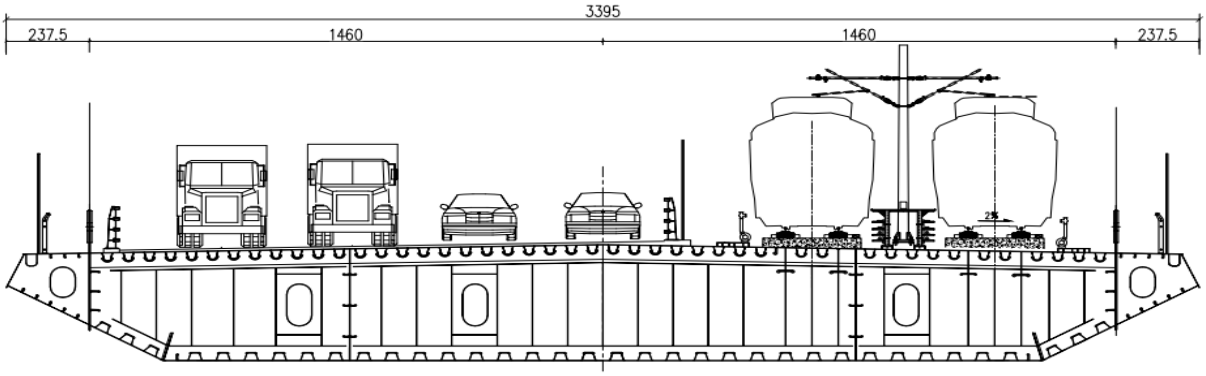

Figure 2. Cross-sectional layout of the main beam (unit: cm).

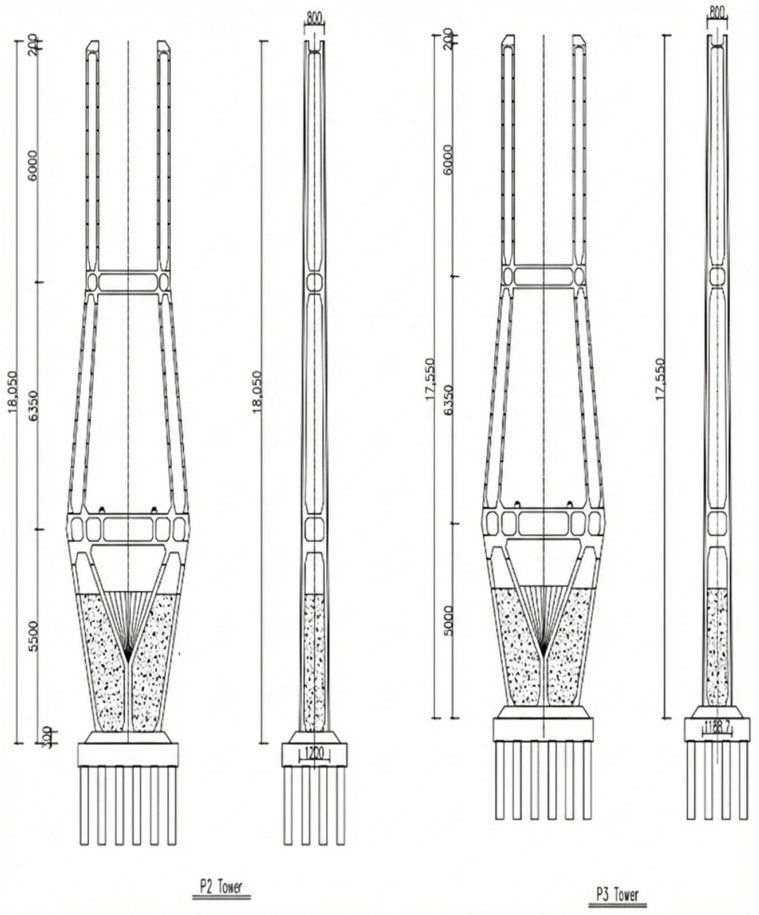

Figure 3. Main tower cross-sectional view (unit: cm).

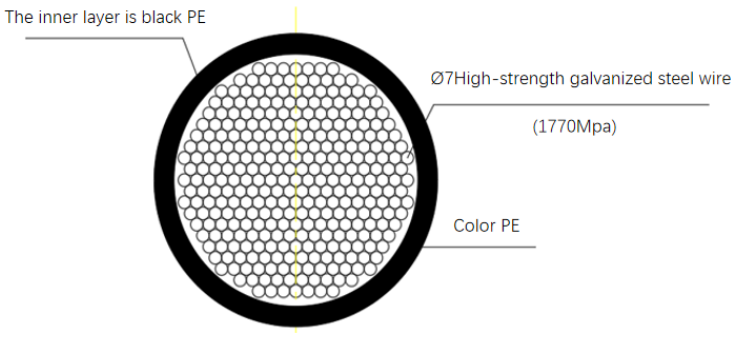

Figure 4. Cross-sectional view of the cable-stayed cable.

4. Finite Element Model

4.1. Full-Bridge Finite Element Model

To study the mechanical characteristics of the main girder of the Li Jiaduo Yangtze River Dual-Channel Bridge, the finite element calculation model of the bridge was established using MIDAS/Civil with the base of the P2 tower as the coordinate origin (as shown in Figure 5). The longitudinal direction of the bridge is the X direction, the transverse direction is the Y direction, and the vertical direction is the Z direction. The model consists of 1074 nodes and 891 elements. The end anchorage zone of the stay cables adopts the modeling method where the cable end nodes and the beam end/tower end nodes coincide, and the displacement coordination is achieved through the rigid connection in the elastic connection. The processing of this connection node essentially aims to avoid the weakening of the lateral and torsional constraints of the cable–bridge–tower system, thereby causing the calculated lateral displacement and torsional response to be larger. The loads of the bridge mainly include the following: the first-phase permanent load (the age of concrete creep is considered to be 30 years based on the service life), the second-phase permanent load and vehicle live load (vehicle live load and train live load), lateral wind load, and temperature load. The stay cables, tower and main girder are simulated using truss elements and beam elements respectively. Boundary constraints are as follows: the tower is fixed at the base, the bridge piers are fixed at the bottom, the main girder is unconstrained in the transverse direction, and the vertical and transverse directions are constrained at the bridge piers and towers. The stay cables, tower, and main girder are connected by the rigid connection in the elastic connection. The mechanical parameters of each component (Q345q steel and C50 concrete) are reasonably selected based on relevant literature and specifications, and the parameters, such as elastic modulus, have a small variation range, which has a limited impact on the overall stiffness of the structure. See Table 1 for details.

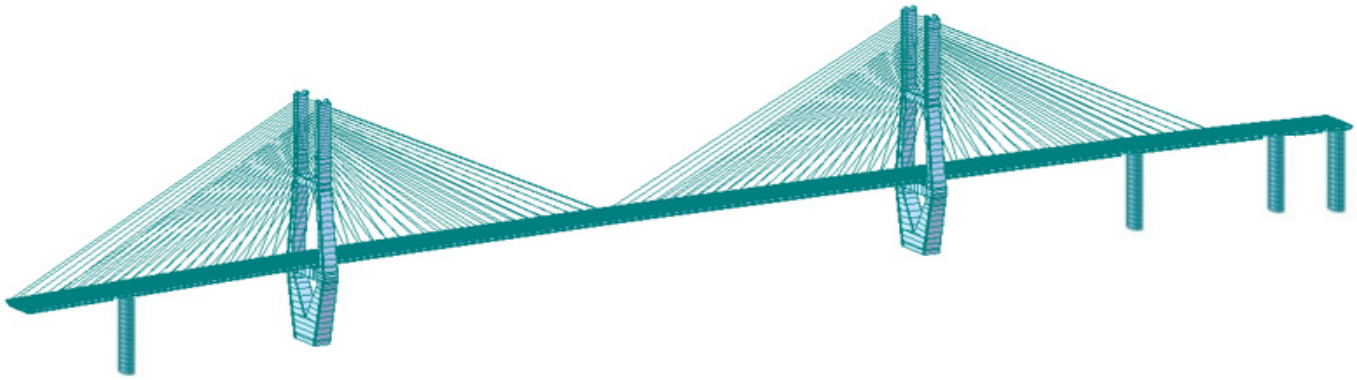

Figure 5. Finite element numerical analysis model of Lijiatuo Yangtze River Double-Line Bridge.

Table 1. Mechanical properties of materials.

Component	Material	Poisson's Ratio	Elastic Modulus/Mpa
Main bridge steel box girder and cable tower	Steel Q345q	0.3	2.10×10^5
Cable-stayed cable	Zinc–aluminum parallel steel strands	0.3	2.05×10^5
Auxiliary pier, junction pier	C40 Concrete	0.3	3.25×10^4
Sota lower tower column anti-collision filling	C25 Concrete	0.2	2.80×10^4
Other padding of the Sota	C50 Concrete	0.2	3.45×10^4

4.2. Local Finite Element Model

Given that the full bridge finite element model has limitations in reflecting the local effects of the structure, and the mid-span closure section, as a key part of this type of bridge, requires a detailed analysis, the MIDAS FEA NX software was used to establish a local finite element model for this closure section. The coordinate system of the model is defined as follows: the longitudinal direction of the bridge is the Y direction, the transverse direction is the X direction, and the vertical direction is the Z direction. The total length of the model is 12 m, and it is divided into three sections along the longitudinal direction. Section 2 (S2) is the main research object and is simulated using 150 plate elements. The mesh type is a mixture of triangles and quadrilaterals, with a size control of 30 mm. To accurately simulate the actual stress state of the mid-span closure section, the boundary conditions at the end sections of the longitudinal direction of the model are fixed; that is, all nodes' six degrees of freedom (DX, DY, DZ, RX, RY, RZ) are constrained. This boundary condition setting is based on the analysis results of the entire bridge: this area is less directly constrained by the bridge tower and is rigidly connected with adjacent beam sections. The fixed constraints can reasonably reflect the constraint effect provided by the adjacent beam sections. In terms of loads, the main factors considered are self-weight, vehicle live load, lateral wind load, and temperature load. The local finite element model is shown in Figures 6 and 7, and the specific material and size information of each plate element is detailed in Table 2.

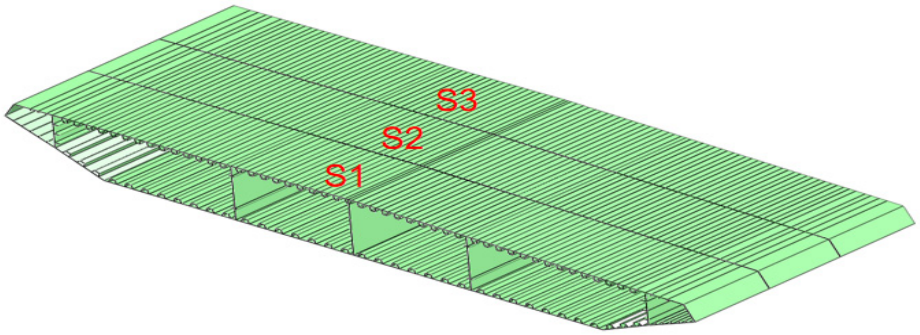

Figure 6. Partial model of the closing section of the Jiatuo Yangtze River Double-Line Bridge.

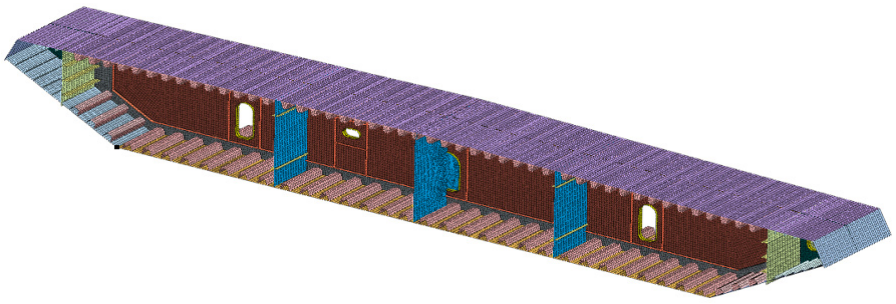

Figure 7. Mesh division of the S2 segment model.

Table 2. Unit material dimensions.

Name of Plate Component	Size and Thickness/mm
Steel box girder top slab	16
Bottom plate of steel box girder, transverse stiffening ribs	24
Reinforced U-rib	8
Wind nozzle, vertical stiffener, steel box girder side bottom plate	10
Web plate	18
Side web	30
Diaphragm construction	12

5. Full Bridge Numerical Simulation

Based on the aforementioned theoretical research and engineering overview, this section establishes a full-bridge finite element model and systematically conducts structural response analysis under operational loads (live load, static wind, and system temperature differences), focusing on revealing the spatial mechanical behavior and response characteristics of the asymmetrical cable-stayed bridge under operational conditions.

5.1. Live Load Numerical Simulation

5.1.1. Analysis of Live Load Values

Under vertical loads, the integral steel box girder exhibits both longitudinal and transverse bending deformation characteristics. Due to the significant differences in the loading patterns between highways and rail transit, the stress mechanism of the integral steel box girder is more complex. The operating hours of Chongqing Rail Transit Line 18 are from 06:30 to 23:48. During this period, the special nature of the combined road–rail bridge leads to differences in the loading time on the road side and the rail side, thereby causing a significant bias load effect. Based on this, and in accordance with relevant specifications and the design requirements of the main bridge, the uniform load and concentrated load are used to simulate the lane load for calculation. The standard value of the uniform load for the I-level lane on the highway is 10.5 kN/m, and the concentrated load is taken as 360 kN. The rail load adopts the national standard as-type vehicle, with a vehicle fixed distance of 13.4 m and a fixed axle distance of 2.2 m, and the axle load range is 80 kN to 150 kN. The impact coefficient is taken as 0.051. To comprehensively assess the structural stress state, three working conditions are considered, as shown in Table 3 and Figure 8: Condition one is double-track rail train fully loaded, without vehicle load; Condition two is single-direction four-lane fully loaded, without train load; Condition three is in accordance with Article 5.3 of the "Code for Design of Urban Rail Transit Bridge" [14], whereby, for components that simultaneously bear rail transit and road loads, the values should be taken based on the most unfavorable combination. This paper takes the fully loaded vehicle load + 0.85 times the fully loaded rail train load.

Table 3. Load Application Condition.

Load Condition	Highway Vehicle Load	Rail Train Load
Operating condition one	None	Fully loaded
Operating condition two	Fully loaded	None
Operating condition three	1.0 vehicle load	0.85 train load

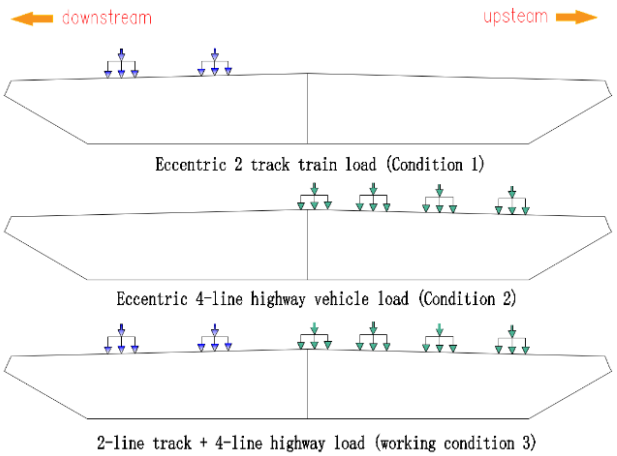

Figure 8. Loading conditions of different moving loads.

5.1.2. Live Load Effect Analysis

A full-bridge finite element model of the Lijiatuo Yangtze River Double-Line Bridge was established based on MIDAS/Civil, and three types of live load combination scenarios were set for loading calculations, all applied along the entire bridge span. The lateral displacement variations of the beams under different live load combinations were analyzed, with the calculation results shown in Figure 9.

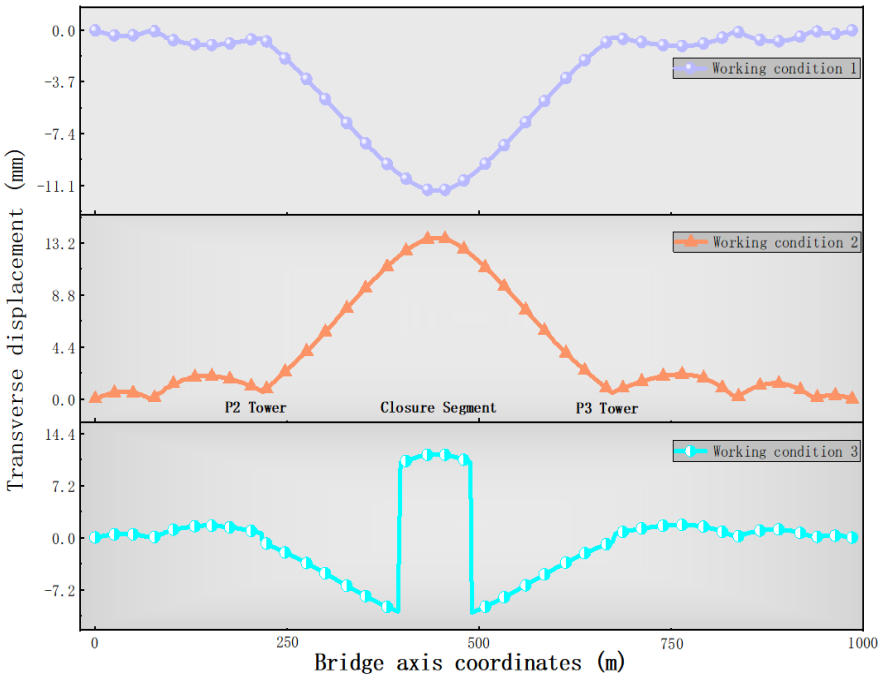

Figure 9. Displacement values under live load.

The analysis shows that the lateral displacement response of the side spans of the main bridge is relatively small under different working conditions, with the maximum value being 2.1 mm (condition two). The lateral displacement of the middle span increases gradually from the abutment towards the mid-span, reaching its maximum at the closure section. Specifically, when condition one (full load of double-track railway) and condition two (full load of one-way four-lane road) are applied, due to the opposite eccentricity ratio e, opposite torques are generated, causing the middle span of the main girder to exhibit reverse lateral deformation (with the maximum displacements being −11.51 mm and 13.64 mm respectively)—directly confirming the mechanical characteristics of asymmetric arrangement—and the displacement increase in condition two reaches 18.6%, reflecting the more significant contribution of multi-lane vehicle loads. The displacement at the auxiliary pier is effectively constrained within the range of 0.07 to 0.21 mm. Particularly, in the middle span section approximately 85.9 m long, a local response opposite to the overall trend occurred, and the displacement curve near the mid-span presented a "discontinuous sudden change" form. After analysis, in this combined working condition, the eccentric directions of the road lane loads and the railway train loads are opposite (the railway train load is reduced by 0.85), so the torsional effect changes its sign along the span, resulting in reverse lateral displacement near the closure section at the mid-span.

Based on the analysis of the spatial lateral deformation characteristics of the beam, the changes in the spatial stress distribution state of the beam were studied. The envelope diagrams of the stress distribution changes of the main bridge under different working conditions were extracted, as shown in Figure 10.

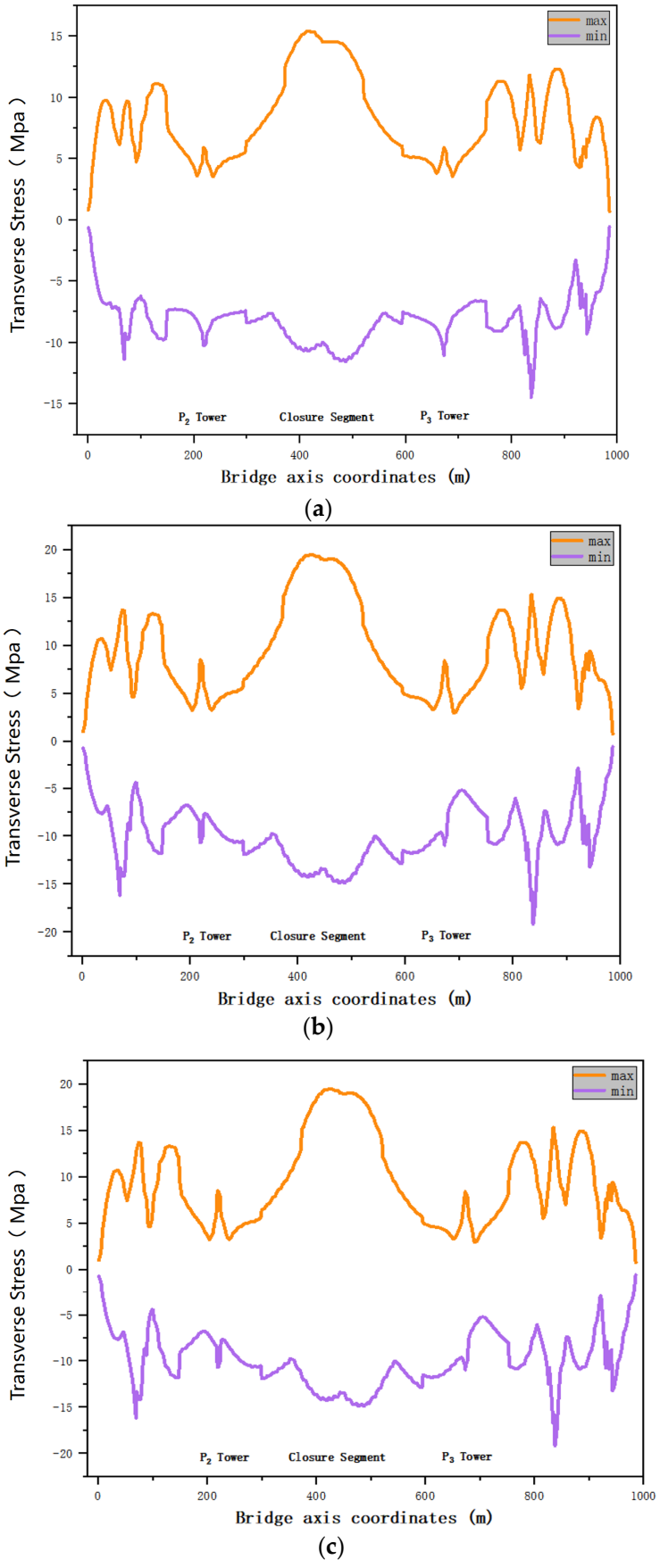

Figure 10. Stress envelope diagram of the main bridge under different moving load conditions. (**a**) Stress envelope diagram of the main beam under working condition 1. (**b**) Stress envelope diagram of the main beam under working condition 2. (**c**) Stress envelope diagram of the main beam under working condition 3.

From the stress envelope diagram in Figure 10, it can be seen that the stress distribution of the main beam exhibits significant spatial non-uniformity: The stress amplitude along the longitudinal direction of the bridge axis shows a distribution pattern of "edge span oscillation–middle span concentration," because the shear lag effect under asymmetric loading coupled with bending and torsion causes ψ(y) in certain areas to increase significantly, resulting in local stress being much greater than the calculated value of the elementary beam theory. This is especially true near the complex constrained edge spans and the stiffening sections with sudden stiffness changes in the middle spans. The stress responses to different load forms vary. The stress amplitude in the mid-span area caused by the track train load (condition one) is 19.7–26.6% higher than that caused by the road vehicle load (condition two), because the track train load, due to its larger axle load and impact effect, generates significantly greater stress in the mid-span area than the road vehicle load. The stress extremes in the combined load condition (condition three) are significantly greater than those in the single load condition, with the maximum tensile stress occurring at the 11/25 L1 section, with a value of 20.8 MPa, representing an increase of 35.1% compared with condition one. After comprehensively considering the lateral displacements under various live loads and the stresses of the main beams, the main beams at the P1 and P4 auxiliary piers, the mid-span of the main span, 9/20 L1, and 11/25 L1 were selected as control sections to analyze the lateral stresses under different moving load conditions. The results are shown in Tables 4–6.

Table 4. Lateral Stress under condition 1.

Control Section	Stress at the Edge of the Lane/MPa	Stress at the Bottom Edge of the Lane/MPa	Stress on the Upper Edge of the Rail/MPa	Stress at the Lower Edge of the Rail/MPa
P1 auxiliary pier	8.98	−11.42	8.99	−11.44
P4 auxiliary pier	10.83	−14.51	11.00	−14.44
Midspan of the main beam	−8.74	14.51	−10.11	13.32
9/20 L1	−9.37	15.11	−10.51	13.88
11/25 L1	−9.68	15.42	−10.74	14.36

Table 5. Lateral stress under operating condition 2.

Control Section	Stress at the Edge of the Lane/MPa	Stress at the Bottom Edge of the Lane/MPa	Stress on the Upper Edge of the Rail/MPa	Stress at the Lower Edge of the Rail/MPa
P1 auxiliary pier	12.41	−16.21	12.43	−16.25
P4 auxiliary pier	14.00	−19.03	13.72	−19.23
Midspan of the main beam	−13.54	16.39	−10.21	19.03
9/20 L1	−14.09	17.08	−11.31	19.54
11/25 L1	−13.57	16.64	−10.61	19.22

Table 6. Lateral stress under operating condition 3.

Control Section	Stress at the Edge of the Lane/MPa	Stress at the Bottom Edge of the Lane/MPa	Stress on the Upper Edge of the Rail/MPa	Stress at the Lower Edge of the Rail/MPa
P1 auxiliary pier	13.12	−17.00	13.22	−16.87
P4 auxiliary pier	15.41	−20.82	15.36	−20.82
Midspan of the main beam	−13.49	19.63	−13.11	19.79
9/20 L1	−14.22	20.03	−13.79	20.44
11/25 L1	−14.73	20.68	−14.29	20.81

From the analysis of Tables 4–6, it can be concluded that, under different working conditions, each control section exhibits consistent stress patterns: the P1 and P4 auxil-

iary pier sections show the characteristics of a negative bending moment cantilever beam (with tension on the upper edge and compression on the lower edge), while the remaining sections present the characteristics of a positive bending moment for a simply supported beam (with compression on the upper edge and tension on the lower edge). Under the combined effect of live loads, the stress differences between the lane and the upper edge of the track are relatively small, ranging from 0.01 MPa (in condition one, P1 auxiliary pier) to 3.33 MPa (in condition two, at the mid-span of the main span). The stress difference on the lower edge ranges from 0.02 MPa to 2.64 MPa, with the extreme values occurring at the corresponding sections to the upper edge.

From the perspective of the response nature, the above distribution reflects the complex stress behavior of the cable-stayed bridge under asymmetric loading: the mid-span area exhibits the stress pattern of a simply supported beam, while at the auxiliary piers, due to the constraints, it forms a cantilever beam stress state. Among these, the combined load (Case 3) has a significant superposition effect on the stress, and in the area near the closure section, due to the relatively weak transverse torsional stiffness, it becomes a stress concentration area. The stress difference between the lane and the track further confirms the bias loading effect caused by the asymmetric distribution of live loads and its nonlinear influence on the internal force distribution. From the mechanical mechanism perspective, this response originates from the bending–torsion coupling effect caused by the eccentric load. The eccentric distance of the combined lateral load force relative to the section stiffness center determines the magnitude of the torque, resulting in simultaneous lateral bending and torsion of the section. The superposition of torsional shear flow and lateral bending shear flow increases the gradient of the shear flow in the near-load side flange and restricts the diffusion of the edge shear flow to the far side, i.e., the shear lag effect. At the constraint abrupt change points (such as the main tower, auxiliary piers, and closure section), the redistribution of constraint torsion and local shear flow further enhances the coupling effect in the longitudinal local area. Therefore, the "edge span oscillation–mid-span concentration" distribution of the stress envelope (Figure 10) is the result of the combined action of lateral bending, torsion, and shear lag, rather than a single bending effect.

Based on the above analysis, in the design and operation phases, special attention should be paid to the local stress control of the closure section and the auxiliary piers area. In particular, the phenomenon of compressive stress concentration at the P4 auxiliary pier should be monitored. It is recommended to strengthen structural monitoring and maintenance in the corresponding sections, and take targeted measures to improve the stress distribution, thereby effectively preventing fatigue or instability risks that may be triggered under long-term load conditions and ensuring the safety and durability of the bridge throughout its entire service life.

5.2. Numerical Simulation of Wind Load Under Calm Conditions

5.2.1. Analysis of Wind Load Values

The dominant wind direction at the bridge site throughout the year is north wind, with a frequency of approximately 13%. In summer, the wind direction is mainly northwest, with a frequency of about 10%. The annual average wind speed is approximately 1.3 m/s, and the maximum wind speed is 26.7 m/s. The wind load is taken according to the provisions of the "Code for Design of Urban Rail Transit Bridge" [14] and the "Bridge Wind Resistance Code for Highways" [15]. Ultimate wind force: Basic wind speed 27.5 m/s.

Therefore, after referring to the above specifications and related reference [16], in this section, when the wind direction is perpendicular to the driving direction, the most unfavorable wind load is applied. The basic wind speeds are 5 m/s, 10 m/s, 15 m/s, 20 m/s,

25 m/s, and 30 m/s, and are loaded in six grades. The transverse displacement and transverse stress of the bridge under different wind speed loads are compared and analyzed.

5.2.2. Lateral Static Wind Load Effect

The results of the bridge's lateral displacement under different wind loadings with varying main beam spans are shown in Figure 11.

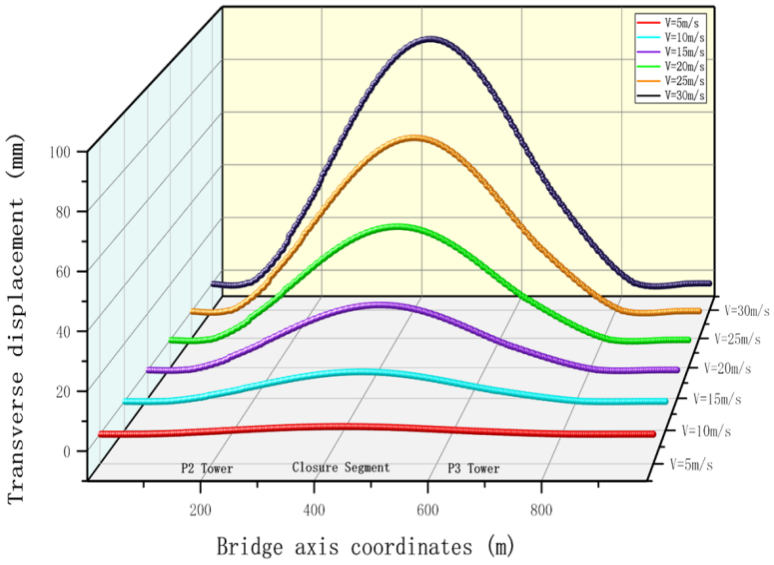

Figure 11. Transverse displacement of the main bridge under different wind loads.

As shown in the above figure, the transverse displacement of the main bridge increases with the increase of wind speed under level 6 loading, with a maximum value of 91.8 mm under level 6 wind load. Under transverse wind load, there is a significant difference between the transverse displacement of the side spans and the middle span. When the wind speed is 30 m/s, the maximum transverse displacement of the side spans is 39.5 mm, while the maximum transverse displacement of the middle span is approximately 2.3 times larger than that of the side spans; thus, the displacement of the side spans is significantly smaller than that of the middle span. When the wind speed is 25 m/s, the maximum transverse displacement of the Jiulongpo side span is 28.3 mm, while that of the Banan side span is 23.8 mm, a decrease of about 15.9%. Under different wind loads, the maximum transverse displacement is concentrated near NJ19 in the cable-stayed section of the middle span, about 16.7 m from the closure section of the middle span. The reason for the above phenomenon is the presence of auxiliary piers, which, by supporting the stay cables and bridge deck load, can reduce the deformation and vibration of the bridge and improve overall stability; at the same time, the auxiliary piers can disperse the wind force acting on the main towers, reducing the stress and deformation on the main towers and enhancing structural stiffness, thereby improving the wind resistance of the bridge. This also causes the transverse displacement of the side spans to be significantly smaller than that of the middle span. In addition, the Jiulongpo side span has only one auxiliary pier, P1, while the Banan side span has two auxiliary piers, P4 and P5. The increased number of auxiliary piers strengthens the transverse stiffness of the side spans and further enhances their wind resistance, leading to the aforementioned situation.

Figure 12 shows the variation of main beam stress under different wind speed loads. As can be seen from Figure 12: with the increase in the wind speed loading level, the stress response of the main beam also increases. This is because the lateral force generated by the wind load on the main beam creates a bending moment, causing the main beam to

bend, which in turn leads to an increase in tensile and compressive stresses, ranging from 0 to 10.7 MPa. Under lateral wind load, the stress variation of the main beam over the entire bridge exhibits an irregular and unstable pattern. When the wind speed reaches 30 m/s, the maximum tensile stress is 10.7 MPa, and the maximum compressive stress is 7.9 MPa, with both maximum values located on the side span on the Jiulongpo side, at distances of 68.8 m and 52.8 m from pier A0, approximately 8/25 L and 6/25 L of the span length, respectively. Further analysis shows that, in the side span 178.2 m away from the P3 tower, the maximum tensile and compressive stress values are 8.1 MPa and 6.4 MPa, which are 24.3% and 19% smaller than those on the side span of the P2 tower, respectively. The maximum tensile stress in the mid-span is 9.4 MPa, located between the cable-stayed sections NJ19 and NJ20 in the cable zone of the mid-span, 14.9 m from the mid-span closure segment (point k in the figure). In addition, the maximum stress observed at the mid-span location is tensile stress, with a value of 9.3 MPa.

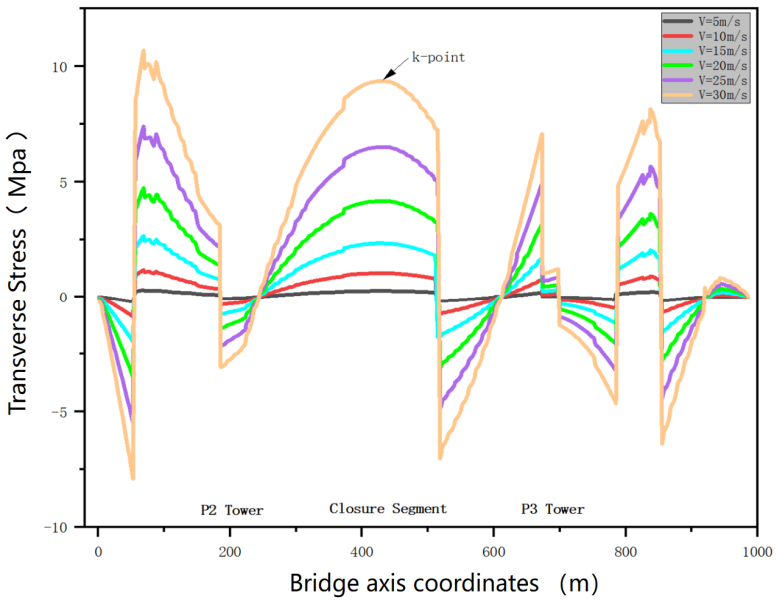

Figure 12. Main beam stress under different wind loads.

After considering the lateral displacement and main girder stress response values under different wind load speeds, when the wind speed V = 30 m/s, the sections at 6/25 L, 8/25 L, mid-span of the main span, and point k are taken as control sections to study the lateral stress of the steel box girder under lateral wind load. The results are shown in Table 7 below.

Table 7. Lateral stress under wind load of 30 m/s.

Control Section	Stress at the Edge of the Lane/MPa	Stress at the Bottom Edge of the Lane/MPa	Stress on the Upper Edge of the Rail/MPa	Stress at the Lower Edge of the Rail/MPa
6/25 L	7.92	5.91	−7.92	−5.90
8/25 L	10.71	7.94	−10.71	−7.94
Main span midpoint	−9.30	−6.93	9.30	6.93
k point	−9.37	−6.99	9.37	6.99

According to the analysis results in Table 7, when the lateral wind speed is 30 m/s, the stress characteristics of the main girder at control sections 6/25 L and 8/25 L show tension at the upper and lower edges of the carriageway and compression at the upper and lower edges of the rail. In contrast, the stress distribution at the midspan and K points exhibits the opposite characteristics, with compression at the upper and lower edges of the carriageway

and tension at the upper and lower edges of the rail. Under the action of lateral wind loads, the stress at the upper edge of the carriageway and the upper edge of the rail, as well as the stress at the lower edge of the carriageway and the lower edge of the rail, show a negative correlation at the four control sections. Specifically, at the cross-section of the steel box girder at 6/25 L, the maximum tensile stress at the upper edge of the carriageway is 7.92 MPa, the maximum compressive stress at the upper edge of the rail is −7.92 MPa, and the maximum stress difference between the upper and lower edges of the rail and the carriageway within the same cross-section is 2.77 MPa. This phenomenon primarily occurs at the main girder near the P1 auxiliary pier.

Based on the above research, under the action of lateral wind loads, the structural response of a same-level, asymmetric, long-span steel box girder cable-stayed bridge for both road and rail exhibits significant spatial non-uniformity and load sensitivity. Auxiliary piers enhance local stiffness, effectively restraining lateral deformation of the side spans; the main span, due to its large span and weak lateral wind resistance stiffness, shows nonlinear response growth with wind speed, and the closure segment experiences stress concentration due to insufficient torsional resistance. In view of this, during the design phase, the influence of auxiliary pier layout on overall wind resistance performance should be fully considered, and, during operation, monitoring should focus on vulnerable regions such as areas with large stress differences and cable zones of the main span, tracking their lateral displacement and stress variations.

5.3. Numerical Simulation of Temperature Effect

5.3.1. Analysis of Temperature Load Values

The temperature for the closure of the bridge is set at 18 °C to 23 °C. Based on the "Urban Rail Transit Bridge Design Specifications" [14], considering regional climate records, structural safety redundancy, and engineering experience, this is a commonly used method in bridge design. The overall heating is considered as 43 °C − 18 °C = 25 °C, and the overall cooling is considered as 23 °C − (−1.8) °C = 24.8 °C ≈ 25 °C.

The lateral displacement of the main bridge under the temperature difference of the system is shown in Figure 13. Here, "+" indicates the displacement (on the track side) perpendicular to the direction of the bridge towards the east, and "−" indicates the displacement (on the lane side) perpendicular to the direction of the bridge towards the west.

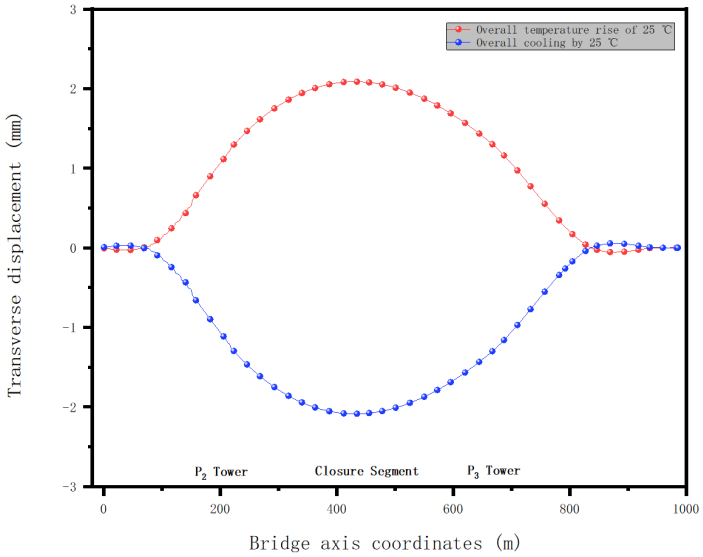

Figure 13. Transverse displacement of the main bridge under system temperature difference.

5.3.2. System Temperature Effect

The lateral displacement of the main bridge under system temperature difference is shown in Figure 13. Here, "+" indicates displacement perpendicular to the bridge span towards the east side (track side), and "−" indicates displacement perpendicular to the bridge span towards the west side (roadway side).

As shown in Figure 13: the transverse displacement of the main girder due to overall temperature rise is very small, with the maximum displacement values for each span being −0.09 mm, 2.13 mm, and −0.11 mm, respectively, showing an overall 'convex' trend. As the main girder is constrained at the piers and cable towers in the transverse bridge direction and cannot deform or expand freely, the displacement of the main girder is relatively small at the P2 and P3 towers, being 1.25 mm and 1.33 mm, respectively. Additionally, auxiliary piers P1, P4, and P5 will experience contraction due to temperature effects, so the corresponding main girder displacement values are close to but not zero. The overall main bridge structure exhibits an eastward shift, with the maximum value of 2.13 mm occurring near the midspan closure segment of the main span. This is because the closure segment is located in the medium-span area of the bridge with a larger span and is a non-cable segment beam, which experiences less constraint; thus, when the temperature changes, the structural effects are amplified in the closure segment. Therefore, the transverse displacement near the closure segment is more pronounced. The cooling effect of the system follows the opposite pattern to that of the warming effect.

The stress on the main beam under the system temperature difference is shown in Figure 14. Here, "+" indicates tension and "−" indicates compression. With an overall temperature change of 25 °C, the system temperature difference causes the structure to tend to elongate or shorten. When the structure is constrained by boundaries, internal restraint forces are generated, causing the stress distribution on the main beam of the cable-stayed bridge to become more complex when constrained by supports, stay cables, etc. Therefore, the stress variations in the main beam are irregular. Under overall heating, the stress range in the main beam is from −8.0 MPa to 7.9 MPa. Due to a sudden stress change occurring at the extreme value location on the Jiulongpo side span, both the maximum and minimum values occur on that side span, at approximately 3/10 L and 3/5 L respectively (L is the length of the main beam from the model beam end to the P2 tower). The reasons for the sudden change are as follows:

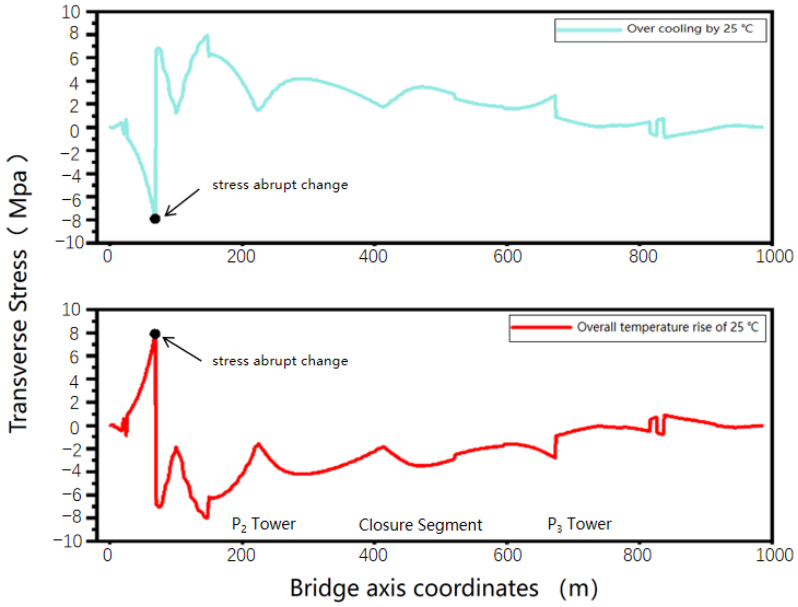

Figure 14. Main beam stress under system temperature difference.

As shown in Figure 15, under the influence of temperature rise and self-weight, the cable-stayed cables undergo elongation and contraction changes. The main span on the Jiulongpo side experiences significant deflection, while the displacement changes of the side span and main span on the Banan District side are relatively small. Figure 16 shows that, under system temperature rise, the cable forces of the NA20–NA01 cables on the side span of the Jiulongpo side exhibit a 'normal distribution' pattern, with the maximum cable force generated by cable NA13 reaching 199.8 kN. The cable forces from the beam end to the P1 auxiliary pier are relatively small, thus having a minor impact on the main beam in this section. Moreover, the cable forces corresponding to NA12–NA14 at the P1 auxiliary pier are larger compared with other NA cables on the side span of the Jiulongpo side, and, since the P1 auxiliary pier has vertical constraints with the main beam, the deformation is minimal. Therefore, the deflection changes of the side span on the Jiulongpo side shown in Figure 15 occur. Ultimately, the main beam from the P2 tower side to the mid-span and the main beam from the A0 beam end to the P1 auxiliary pier compress against each other, causing a sudden stress change at this location and leading to maximum and minimum stress values.

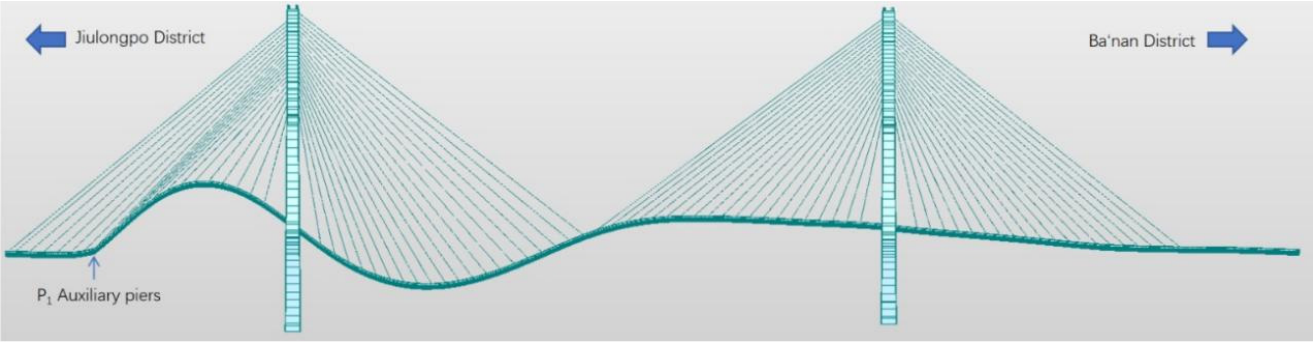

Figure 15. Vertical deformation of the main beam with an overall temperature increase of 25 °C.

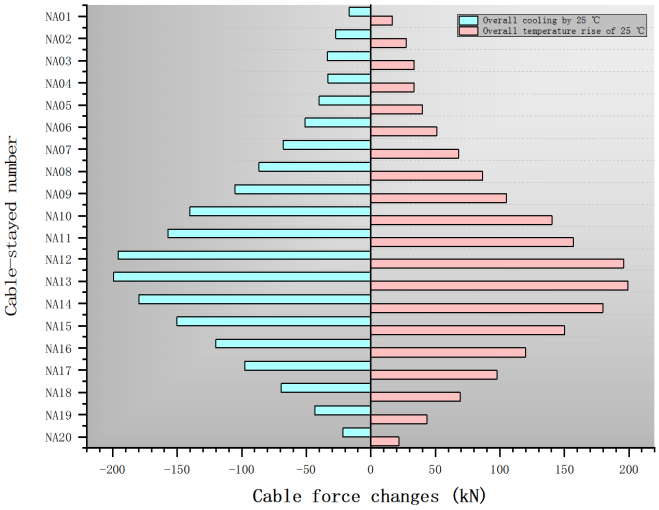

Figure 16. Variation of cable force under system temperature difference.

Due to the symmetrical response of the structure to an overall temperature increase and decrease of 25 °C, only the temperature increase is studied during stress analysis. Therefore, after considering the transverse displacement and main girder stress under the temperature differential of the system, the sections at 3/10 L, 3/5 L, midspan of the main span, and midspan of the Ban'an side span are chosen as the control sections for analyzing the transverse stress under the temperature rise effect of the system, as shown in Table 8.

Table 8. Lateral stress of the system at a temperature increase of 25 °C.

Control Section	Stress at the Edge of the Lane/MPa	Stress at the Bottom Edge of the Lane/MPa	Stress on the Upper Edge of the Rail/MPa	Stress at the Lower Edge of the Rail/MPa
3/10 L	−6.08	7.92	−6.81	7.38
3/5 L	3.34	−7.83	3.11	−8.01
Main span midpoint	0.73	−3.21	0.51	−3.04
Central span on the south side of Banan	−0.14	0.72	−0.75	0.26

From Table 8, it can be seen that, under an overall structural temperature rise of 25 °C, and due to the temperature effects being applied to the entire main bridge model, there are many influencing factors, making it extremely complex and in turn causing different effects on main beams at different locations. Therefore, at section 3/10 L and at mid-span of the side span on the Banan side, both are in a simply supported beam positive bending moment stress state, but the response value at mid-span of the side span on the Banan side is small. At section 3/10 L, the maximum lateral compressive stress of the steel box girder cross-section occurs at the top of the tracks, with a value of 6.81 MPa, and the maximum lateral tensile stress occurs at the bottom of the carriageway, with a value of 7.92 MPa. At sections 3/5 L and at mid-span of the main span, the girder is in a cantilever beam negative bending moment stress state; the maximum lateral compressive stress of the steel box girder occurs at the bottom of the track, with a value of 8.01 MPa, and the maximum lateral tensile stress occurs at the top of the carriageway, with a value of 3.34 MPa. In the same control section, the maximum difference at the top edge is 0.73 MPa and the maximum difference at the bottom edge is 0.54 MPa, both occurring at section 3/10 L, which can be considered as the lateral stress being symmetrically distributed under the system's temperature difference.

Compared with ordinary cable-stayed bridges, this bridge, due to the particularity of its non-symmetrical arrangement of the roadway and rail on the same level, exhibits more complex stress characteristics under temperature effects. Its lateral displacement and stress distribution are influenced not only by temperature changes but also show significant asymmetric effects due to the structural asymmetry. Therefore, during the design stage, compared with ordinary cable-stayed bridges, this bridge requires more refined consideration of the structural response under temperature effects, enhancing its temperature adaptability through measures such as optimizing cross-section design and increasing torsional stiffness in key areas. During the operation stage, real-time monitoring of temperature-sensitive areas (such as closure segments and stress change points) should be reinforced to ensure structural safety.

6. Local Numerical Simulation

To thoroughly reveal the spatial effects of an asymmetrical cable-stayed bridge under operational loads, this paper conducts a detailed local analysis focusing on the midspan closure section of the steel box girder as a key part; due to space limitations and for the sake of intuitive indicators, lateral displacement, which can reflect the overall structural deformation trend, is selected as the core evaluation index. The study systematically examines its response under different operational loads to complement full-bridge analysis and to reveal the local spatial mechanical behavior of the steel box girder.

The overall bridge analysis aims to study the macroscopic mechanical behavior of the entire structure under different loads, revealing the general patterns of lateral displacement and stress distribution under live load, static wind, and temperature effects. In contrast, the local analysis focuses on the closure segment at midspan, further examining the displacement response characteristics of the local steel box girder under load, serving as a refinement and complement to the overall bridge analysis. It should be noted that, due

to differences in analysis scale and boundary conditions, the data in this local study may slightly differ from the previously mentioned overall bridge analysis, which is a reasonable phenomenon. The final conclusions will primarily be based on the overall bridge analysis, and the local analysis of the steel box girder in this section is only for supplementary reference, aiming to further reveal the distribution characteristics of the mechanical responses of the steel box girder under loading.

6.1. Live Load Analysis

Based on the live load analysis of the full-bridge analysis mentioned earlier, three load conditions are applied to the local model: Condition 1 for railway vehicle loads, condition 2 for highway vehicle loads, and condition 3 for combined railway and highway vehicle loads. The values are taken according to relevant literature and standards and applied to the model in the form of pressure, as shown in Figure 17.

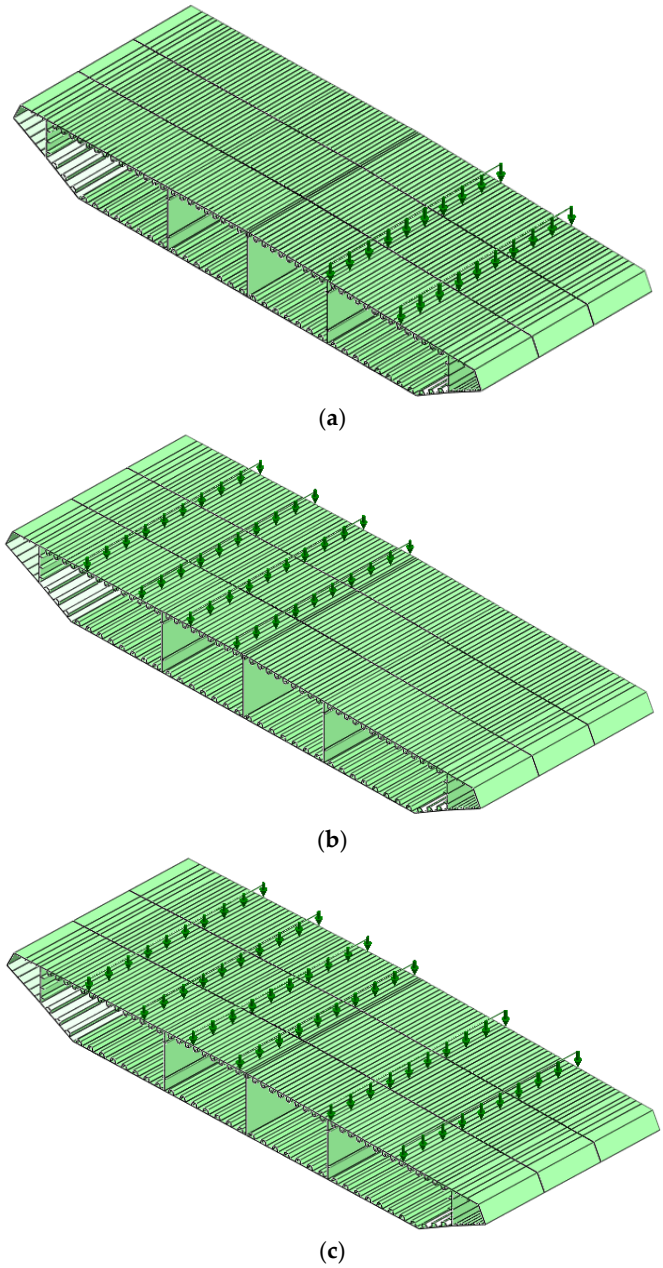

Figure 17. Local analysis live load diagram. (**a**) Track train load application diagram. (**b**) Highway vehicle load application diagram. (**c**) Road vehicle and rail train load application diagram.

Under various working conditions, the lateral displacements generated by the local model of the steel box girder are shown in the figure below.

As shown in Figure 18, under different live load conditions, the steel box girder at the mid-span closure section experiences the largest lateral displacement where the live load acts; under condition 1, the maximum lateral displacement caused by train load occurs on the inner track, ranging from −16.4 mm to −18.5 mm, while the lateral displacement on the outer track ranges from −12.1 mm to −14.3 mm, and the lateral displacement in most areas ranges from −1.5 mm to 0.61 mm; under condition 2, under the action of highway vehicle loads, the lateral displacement values of the four lanes from outer to inner are [9.1 mm, 10.8 mm], [14.3 mm, 16.1 mm], [10.8 mm, 12.5 mm], and [3.9 mm, 5.6 mm], respectively, with the maximum lateral displacement occurring in the second lane, and the middle two lanes showing larger displacements than the edge lanes. This is attributed to the stronger constraints and higher stability of the edge lanes in the structural design, whereas the middle lanes are less restrained, resulting in significant lateral displacement. Under condition 3, under the combined action of train and highway vehicle loads, the lateral displacement values are larger than those under condition 1 and condition 2, with the maximum lateral displacement on the track side being [17.1 mm, 20.5 mm] and on the lane side [16.2 mm, 19.5 mm].

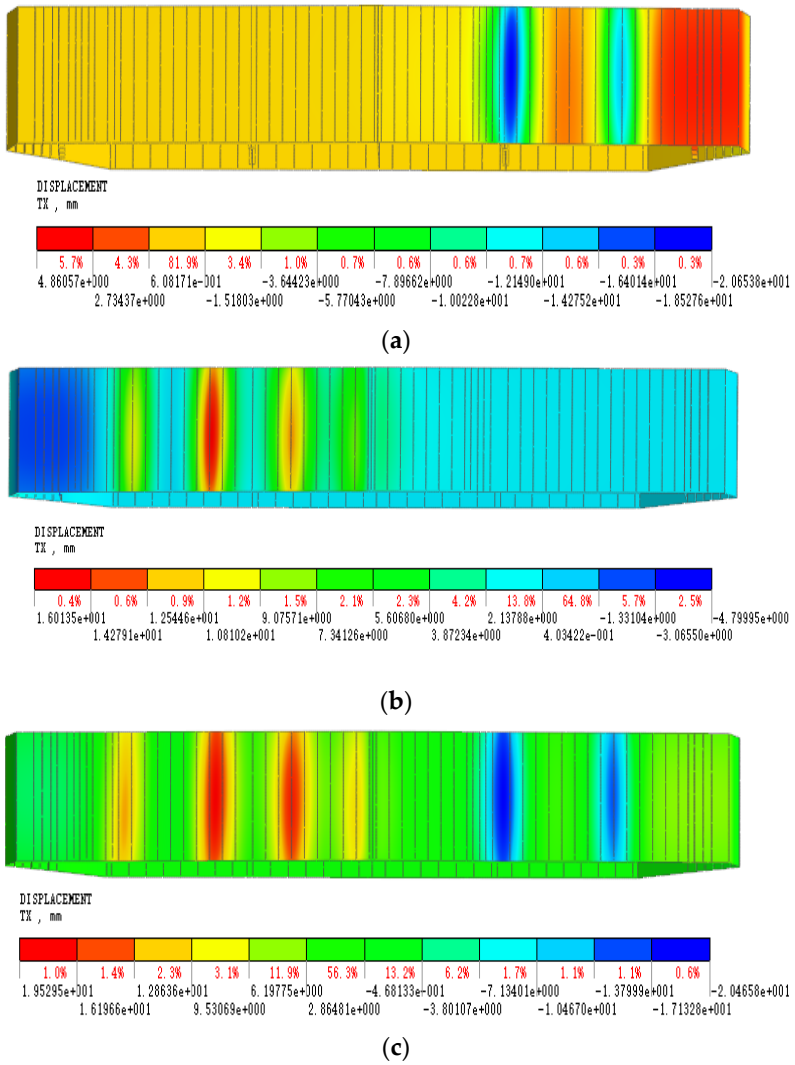

Figure 18. Lateral displacement diagram under local live load. (**a**) Lateral displacement of the rail transit train under load (condition 1). (**b**) Lateral displacement of highway vehicles under load (condition 2). (**c**) Lateral displacement of the track under train load (condition 3).

Through the local live load analysis of the closure segment across the pier, the spatial non-uniformity of the transverse displacement of the steel box girder under live load was revealed, which is closely related to the load distribution. This further deepens the understanding of the local structural behavior of this special bridge type and provides detailed basis for structural optimization and local stiffness enhancement of the closure segment.

6.2. Analysis of Static Wind Load

In this article, the local transverse static wind load is taken with a wind speed of v = 30 m/s, and it is applied as pressure on the local model, as shown in Figure 19. The lateral displacement of the steel box girder in the mid-span closure segment under transverse wind load is shown in Figure 20.

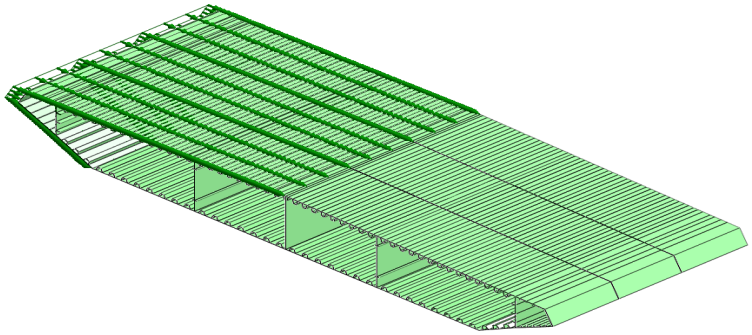

Figure 19. Local analysis lateral wind load application diagram.

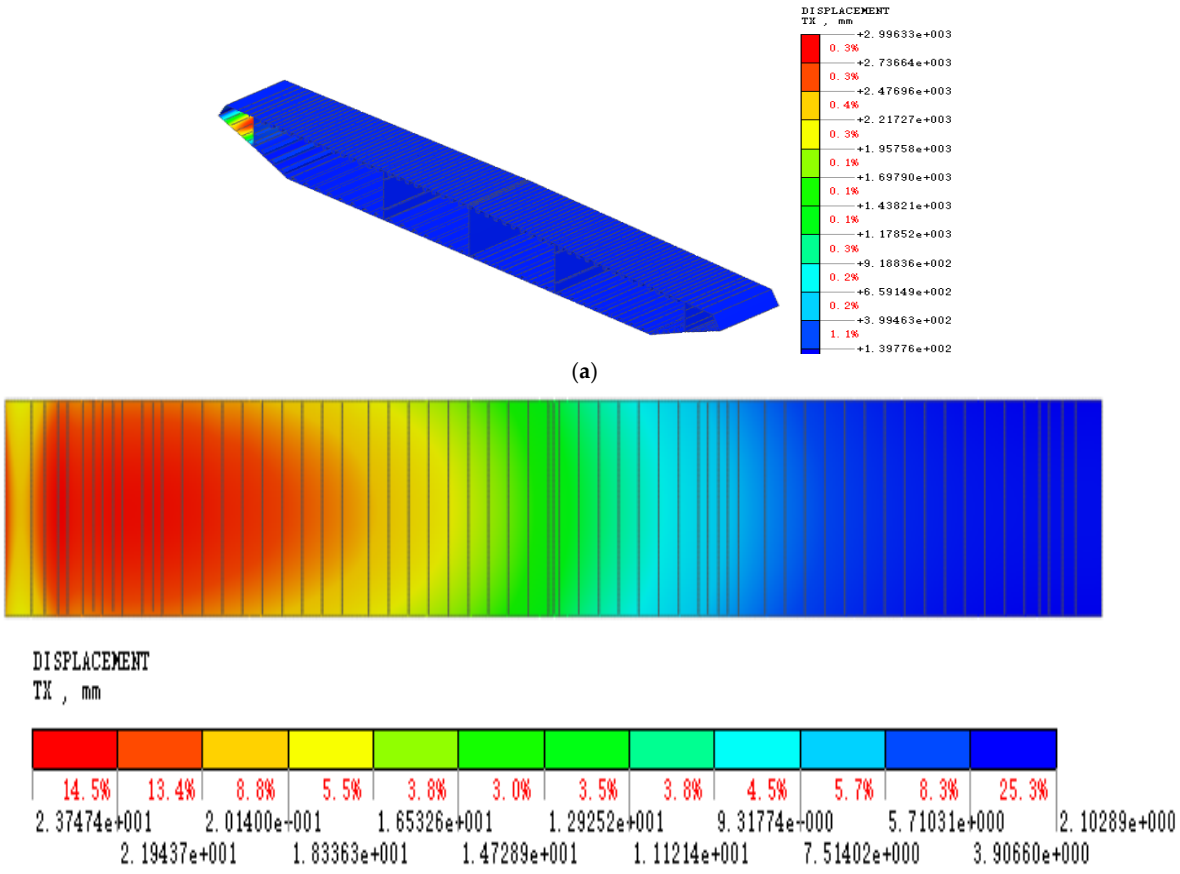

Figure 20. Local analysis lateral wind load displacement diagram. (**a**) Lateral displacement diagram of the full model under lateral wind load. (**b**) Displacement variation of the roof slab under lateral wind load.

According to Figure 20, under a lateral wind load of 30 m/s, the local model exhibits a significant spatially non-uniform distribution of structural displacement, with displacements concentrated in specific areas, ranging from 139.8 mm to 399.5 mm. This non-uniformity is mainly attributed to the boundary condition where the lateral wind load is applied only on the windward side. Analysis shows that the maximum lateral displacement of the windward structure under the lateral wind load reaches 2996.3 mm, about 10 times that of the leeward side displacement (291.4 mm). This result fully indicates that lateral wind load has a non-negligible impact on the bridge structural response.

To further investigate the variation pattern of structural displacement, the top plate of the model was selected for a specialized analysis. By studying the distribution characteristics of the top plate's lateral displacement, it was found that, along the lateral direction from left to right, the displacement shows a clear decreasing trend. Compared with the lateral displacement distribution in localized areas, the displacement distribution of the top plate exhibits higher uniformity, with a maximum displacement of 23.7 mm and a minimum displacement of 2.1 mm.

This local analysis further develops the conclusions of the full-bridge analysis, clarifying that the mid-span closure segment of the steel box girder is a critical stress area under static wind loads. Accordingly, it is recommended that, in the design of the closure segment, particular attention should be paid to the coordination of its lateral stiffness and torsional stiffness, especially the strength of the edge components on the windward side. Consideration can be given to suppressing local deformation by optimizing the spacing of diaphragms or adding local stiffening ribs. In the bridge health monitoring system, displacement and strain sensors should be symmetrically arranged on the windward and leeward sides of the closure segment to monitor long-term displacement differences and stress distribution, providing data support for assessing the cumulative effects of wind-induced fatigue.

6.3. Temperature Effect Analysis

The overall temperature increase of 25 °C was selected as the working condition, and this temperature load was applied to the local steel box girder model through node temperature loading, as detailed in Figure 21. Based on the above loading conditions, the transverse bridge displacement response of the local steel box girder under an overall temperature increase of 25 °C is shown in Figure 22.

The analysis results show that, under the overall temperature increase of 25 °C, the lateral displacement of the mid-span closure section of the steel box girder exhibits a relatively significant symmetrical distribution feature, and the lateral displacement values from the outside to the inside show a decreasing trend. The maximum negative displacement is located on the highway side, with a value of −3.61 mm; the maximum positive displacement occurs on the track side, with a value of 3.57 mm. This is because, on the one hand, the structural symmetry of the mid-span closure section steel box girder makes the thermal expansion and contraction effects on both sides relatively balanced when heated, resulting in a symmetrical lateral displacement. On the other hand, from the outside to the inside, the temperature gradient on the beam body gradually decreases, so the lateral displacement values also decrease accordingly.

This local analysis verifies the conclusion in the overall bridge analysis that the mid-span closure section is the key part for temperature effects, and further indicates, from the microscopic scale, that, although the temperature response of the entire bridge is relatively small, a local symmetrical lateral displacement still appears that cannot be ignored in the closure section. This phenomenon reveals the unique response mechanism of local steel box girders under temperature action. Although the load arrangement is asymmetric, the

structural symmetry of the closure section steel box girder still dominates its local temperature deformation mode, demonstrating the coupling effect between overall constraints and local deformation.

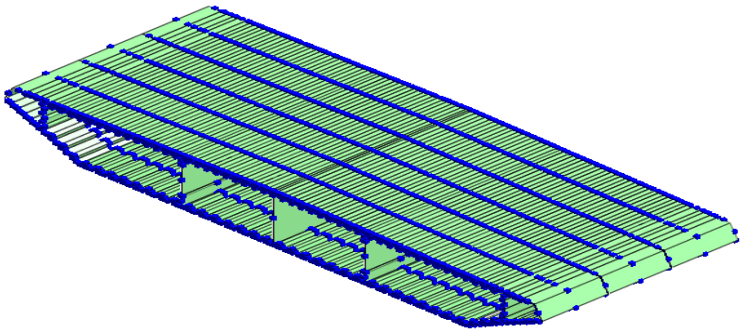

Figure 21. Local analysis temperature load diagram.

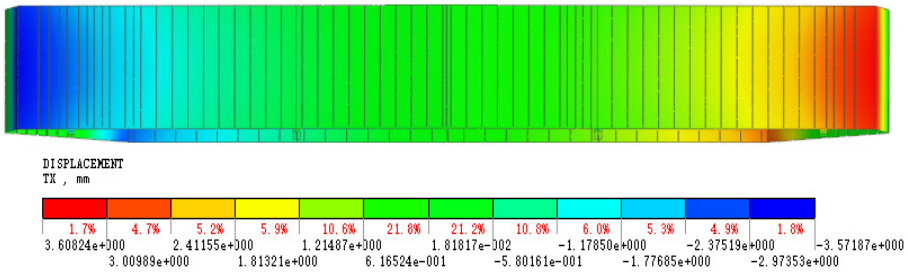

Figure 22. Lateral displacement diagram under a temperature increase of 25 °C.

Based on the above understanding, it is recommended that, in similar bridge design, in addition to paying attention to the overall temperature effect, the design for resisting temperature deformation of the closure section should be further detailed, especially focusing on the configuration of its symmetrical stiffness. During operation, long-term monitoring of the lateral displacement of the closure section should be strengthened to provide data support for evaluating the cumulative temperature effect and the long-term performance of the structure.

7. Monitoring Response Analysis and Its Comparison with Numerical Simulation

7.1. Health Monitoring System

All of the above are based on finite element simulation analysis, lacking actual bridge verification, and there are doubts about their correctness. In view of this, this paper, in accordance with relevant norms [17], will use the monitoring data collected by the health monitoring system to verify the reliability of the full bridge simulation data. Considering that the analysis of the above operational loads (vehicle, wind, temperature) involves the midspan section of the main span, and that the structural response of the main bridge is more significant under live load, and due to space limitations, this paper will separately verify the displacement of the monitored Section 7 of the main girder (midspan section of the main span) under live load in condition 1, as well as the stress at the midspan section under condition 2.

A schematic diagram of the overall layout of monitoring points in the long-term health monitoring system of the Lijiatuo Yangtze River Second Line Bridge is shown in Figure 23 (A represents the main tower monitoring section, B represents the main girder monitoring section, and C represents the cable-stayed monitoring). The monitoring points include ① expansion joint displacement, ② video surveillance, ③ vertical deformation

of the main girder, ④ stress of the main girder, ⑤ temperature of the main girder, ⑥ vibration of the main girder (lateral), ⑦ vibration of the main girder (longitudinal), ⑧ horizontal displacement at the top of the piers, ⑨ bearing reaction, ⑩ GNSS deformation system, ⑪ ship collision (lateral), ⑫ ship collision (vertical), ⑬ ship collision (longitudinal), ⑭ horizontal displacement at the top of the towers, ⑮ wind speed and direction, ⑯ rainfall, ⑰ temperature and humidity, ⑱ vibration of the main tower (lateral), ⑲ vibration of the main tower (longitudinal), ⑳ stress of the main tower, ⑫ temperature of the main tower, ㉒ steel structure fatigue, ㉓ water level, ㉔ cable force monitoring.

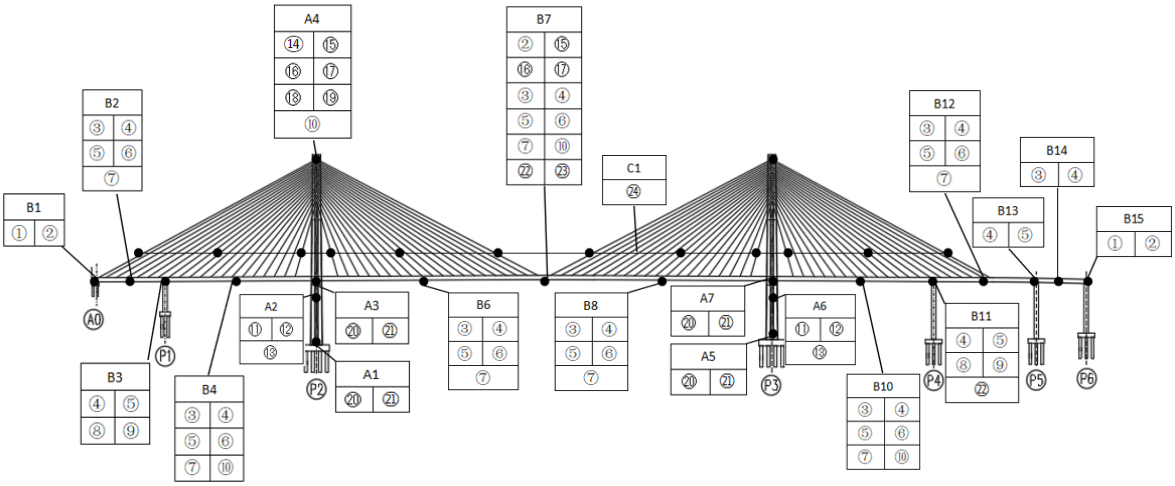

Figure 23. Detailed Layout of Monitoring Section Seven of the Main Beam.

7.2. Monitoring Response Analysis and Numerical Simulation Comparison

This article is based on the GNSS deformation monitoring system and fiber Bragg grating strain gauges of the Lijiatuo Yangtze River Double-Track Bridge. It extracts the transverse deformation data and stress variation data of the mid-span cross-section of the main girder on 24 January 2025, as summarized in Figure 24 and Table 9.

Figure 24a and Figure 24b respectively show the lateral displacement and stress changes of the main span mid-section of the main girder on 24 January 2025. There are obvious fluctuations and numerous peaks, which is because the transient dynamic responses caused by vehicle, train loads and wind loads under the operating state are superimposed on the quasi-static displacement, and GNSS monitoring experiences short-term lockouts, weekly jumps and other measurement noises in complex environments, thus presenting local peaks.

Among them, Figure 24a shows that the lateral displacement of the mid-section of the main span presents dynamic change characteristics under the actual operation state. The maximum lateral displacement to the west (lane side) is −10.9 mm, and the maximum displacement to the east (railway side) is 7.7 mm. Additionally, this typically shows a negative displacement towards the lane side. The maximum displacement value in the first working condition is −11.5 mm, which differs from the maximum displacement value of the monitoring data by 0.6 mm, indicating that the theoretical model has high accuracy. Figure 24b reflects the stress changes of the mid-section of the main span. The data collected by the fiber optic grating strain gauge shows that the stress of this section is all compressive stress, ranging from −11.6 MPa to −5.5 MPa. The maximum compressive stress value in the second working condition is −13.5 MPa, which differs from the maximum compressive stress value of −11.6 MPa of the monitoring data by 1.9 MPa, further verifying the reliability of the theoretical model.

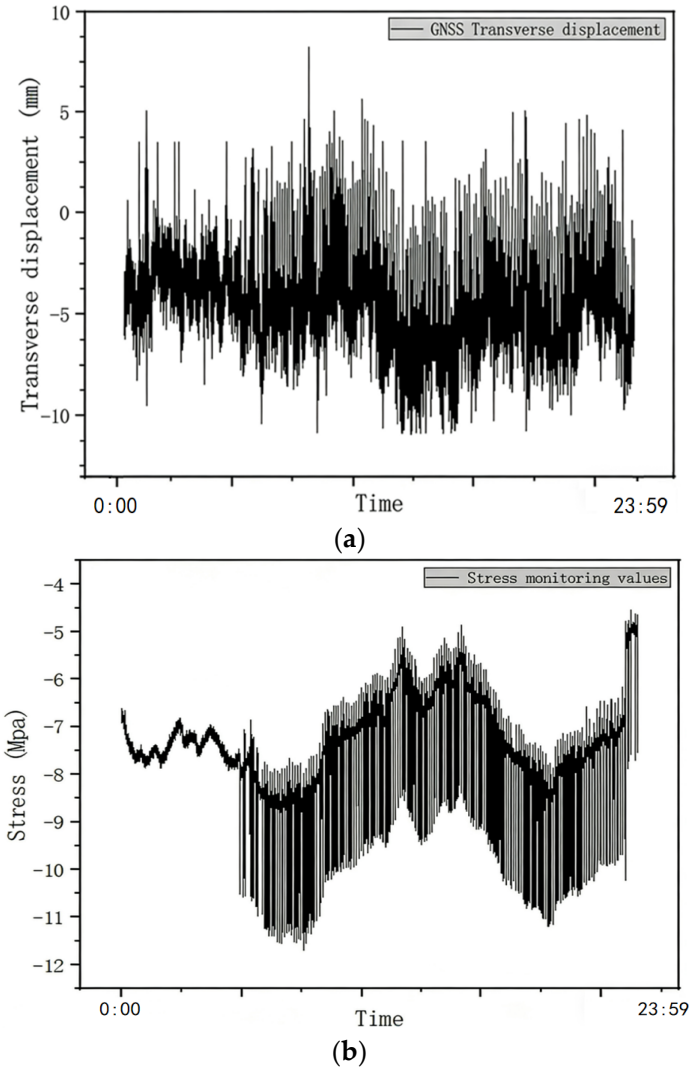

Figure 24. Monitoring data variation chart. (**a**) Transverse displacement variation of the main span midsection (unit: mm). (**b**) Stress variation at mid-span cross-section (unit: Mpa).

Table 9. Comparison of measured and theoretical values of displacement and stress.

Project	Maximum Monitored Value	Maximum Theoretical Value	Difference
Displacement value/mm	−10.9	−11.5	0.6
Stress value/Mpa	−11.6	−13.5	1.9

Overall, the lateral displacement and stress monitoring data of the mid-section of the main span cross-section of the Li Jiaduo Yangtze River Dual-Channel Bridge are highly consistent with the theoretical simulation data, indicating that the theoretical model has scientificity and effectiveness in describing and predicting the mechanical characteristics of the bridge structure.

8. Conclusions and Prospect

This paper takes the Lijiatuo Yangtze River Double-Line Bridge as the background and, by establishing detailed finite element models of the entire bridge and its local parts, systematically studies the mechanical responses of a large-span steel box girder cable-stayed bridge with an asymmetrical arrangement of road and rail on the same level under operational loads (including live load, wind load, and temperature load). The findings are validated using health monitoring data, and the main conclusions are as follows:

1. Numerical simulations of the entire bridge indicate that the eccentric effect of live loads during operation and wind loads are the main factors affecting the structural response. The temporal and spatial asymmetry of the road and track loads leads to reverse lateral displacement of the main beam, with the maximum lateral displacement of the middle span reaching 13.64 mm under the full load condition of the road. The stress distribution shows a non-uniform characteristic of "oscillation at the side spans–concentration at the middle spans," with the maximum tensile stress under the combined load reaching 20.8 MPa. Under the lateral static wind load, the lateral displacement of the main bridge is positively correlated with the wind speed, and the maximum displacement of 91.8 mm occurs near the diagonal cable NJ19 of the middle span, approximately 2.3 times that of the side span. The stress range of the main beam is 0–10.7 MPa. Although the temperature effect causes a relatively small overall displacement (about 2.13 mm), it is prone to cause local stress concentration in the constraint mutation area. The full bridge response shows obvious spatial non-uniformity. The middle span closure section is prone to form stress concentration due to its weak torsional stiffness, while the auxiliary pier shows the characteristic of a cantilever beam. Therefore, for similar asymmetric bridges, it is necessary to focus on the lateral stiffness and torsional construction design of the mid-span closure section and the middle-span cable area, and to conduct the most unfavorable condition verification.
2. Local numerical simulation revealed the response mechanism of the closure section under operational loads. Under the live load condition, the lateral displacement of the middle lane is larger than that of the edge lane, and the combined load effect further increases the extreme displacement value, reaching 20.5 mm. Under the lateral static wind load, the lateral displacement on the windward side is approximately 10 times that of the non-windward side, and the spatial non-uniform distribution characteristic is significant. Under the temperature load, the displacement is symmetrically distributed, with the maximum displacement on the highway side and the railway side being −3.61 mm and 3.57 mm respectively. It is recommended to enhance the ability of local structures to resist deformation under operational loads in key areas, such as the closure segments, by optimizing the layout of diaphragms and stiffening ribs.
3. The health monitoring data indicate that the maximum lateral displacement of the mid-span cross-section of the main span is −10.9 mm, with an error of only 0.6 mm compared with the theoretical value −11.5 mm. The maximum compressive stress monitored is −11.6 MPa, with an error of 1.9 MPa compared with the theoretical value of −13.5 MPa, both of which are within the reasonable range, verifying the accuracy of the finite element model. It is recommended to set an early warning threshold based on this in operation, strengthen real-time monitoring of key areas such as the closure section and auxiliary piers, and improve the level of refined structural safety management.

Although this paper has conducted a relatively systematic numerical analysis and preliminary monitoring verification of the spatial effects of asymmetric cable-stayed bridges under operational loads, there is still room for further in-depth research. In terms of numerical analysis, future research can delve into the evolution law of the response under the coupling effect of multiple factors such as vehicle, wind, and temperature during long-term operation, and adopt dynamic analysis methods to consider the influence of train speed on live load distribution and dynamic amplification. In terms of monitoring data verification, it is difficult to fully reveal the statistical laws by relying solely on deterministic finite element analysis. In recent years, models such as the generalized extreme value

mixture model can model monitoring data with mixed skewness characteristics and predict extreme response states [18], while the Gaussian mixture model provides an effective tool for clustering and interpretable prediction of multi-source monitoring data [19]. Therefore, future research can further combine probabilistic and statistical methods to model long-term monitoring data and predict extreme values, thereby more scientifically assessing the performance evolution and safety risks of the structure under random loads.

Author Contributions: Conceptualization, X.L. and S.X.; methodology, P.D.; software, P.D.; validation, X.L., P.D. and S.X.; formal analysis, X.C.; investigation, Q.W. and M.Z.; resources, M.Z. and X.C.; data curation, M.Z. and X.C.; writing—original draft, Q.W.; writing—review and editing, X.L. and S.X.; visualization, Q.W.; project administration, X.L. All authors have read and agreed to the published version of the manuscript.

Funding: This research received no external funding.

Data Availability Statement: All of the data and models that were generated and used during the study are available from the corresponding author by request. The data are not publicly available due to privacy.

Conflicts of Interest: Authors Peng Ding and Xiaohu Chen were employed by the company T.Y. Lin International Engineering Consulting (China) Co., Ltd. The remaining authors declare that the research was conducted in the absence of any commercial or financial relationships that could be construed as a potential conflict of interest.

References

1. Zhou, M.; Liu, Y.; Deng, W.; Hassanein, M.F.; Zhang, H. Transverse analysis of full-scale precast segmental box girder segments with corrugated steel webs: Experimental tests and FE modelling. *Eng. Struct.* **2019**, *187*, 231–241. [CrossRef]
2. Li, G.; Xiao, L.; Zhang, W.; Wei, X.; Zhao, J.; Wen, Z. Model Test of Ultra-Wide Steel Box Girder Segments of a Road-Rail Flat-Slab Cable-Stayed Bridge and Study on Live Load Effects. *J. China Railw. Soc.* **2023**, *45*, 47–54.
3. Liu, A.; Li, X.; Guo, X.; Ding, P.; Qi, Y. Reasonable Stiffness Limits for Long-Span Track Suspension Bridge. *J. Chongqing Jiaotong Univ. (Nat. Sci.)* **2018**, *37*, 13–20.
4. Zhang, P.; Wen, Y.; Li, Z. Stress and deformation of seamless CWR on large-span cable-stayed bridge under static wind load. *J. Vib. Shock.* **2024**, *43*, 7–13. [CrossRef]
5. Li, S.; Fan, Z.; Chang, Y. Analysis of Lateral Effects of Static Loads on A-Shaped Bridge Towers Without Lower Crossbeams. *Bridge Constr.* **2020**, *50*, 20–25.
6. Mutashar, R.; Sargand, S.; Al Rikabi, F.T.; Khoury, I. Response of a composite-adjacent box beam bridge with skewed beams under static and quasi-static loads. *J. Perform. Constr. Facil* **2019**, *33*, 04019022. [CrossRef]
7. Chen, Y.; Chen, J.; Zhou, C.; Zhai, M. Research on Thermal Effect of Steel-concrete Bonding Section of Cable-stayed Bridge with Wide Hybrid Beam. *J. Wuhan Univ. Technol. (Transp. Sci. Eng.)* **2024**, *48*, 969–973.
8. Deng, W.; Zhang, W.; Liu, D.; Zhang, J. Analysis of Transverse Mechanical Properties of Overlying Concrete Slabs over Steel Girders of Different Cross-Sections. *Bridge Constr.* **2024**, *54*, 116–123. [CrossRef]
9. Hu, H.; Gao, C.; Liu, Y.; Shi, D.; Li, C.; Liu, B.; Ge, Q. Local Stress Analysis of Main Girder of Long-span Railway Prestressed Concrete Extradosed Cable-stayed Bridge with Single Cable Plane. *Railw. Eng.* **2025**, *65*, 63–69.
10. Zhao, H.; Ding, Y.; Nagarajaiah, S.; Li, A.Q. Behavior Analysis and Early Warning of Girder Deflections of a Steel-Truss Arch Railway Bridge under the Effects of Temperature and Trains: Case Study. *J. Bridge Eng.* **2019**, *24*, 05018013. [CrossRef]
11. Crespi, P.; Zucca, M.; Longarini, N.; Giordano, N. Seismic Assessment of Six Typologies of Existing RC Bridges. *Infrastructures* **2020**, *5*, 52. [CrossRef]
12. Deng, H.; Cheng, W. Equivalent Modeling Method for Open Thin-Walled Beams under Transverse Reinforcement Components. *J. Beijing Univ. Aeronaut. Astronaut.* **2016**, *42*, 1469–1478. [CrossRef]
13. Hao, J.; Zhong, W. *Bending and Torsion of Thin-Walled Members*; Higher Education Press: Beijing; Beijing, China, 2006.
14. *Code for Design of Urban Rail Transit Bridge*; Ministry of Housing and Urban-Rural Development of the People's Republic of China: Beijing, China, 2017.
15. *Wind-Resistant Design Specification for Highway Bridges*; Ministry of Transport of the People's Republic of China: Beijing, China, 2018.
16. Chen, B.; Yang, J.; Zhao, H.; Lu, M. Multi-task multi-level alarm of long-span railway bridge monitoring systems via excitation-response indicators cross-cooperation. *High-Speed Railw.* **2025**, *3*, 261–266. [CrossRef]

17. *GB/T 39559.1-2020*; Specifications for Operational Monitoring of Urban Rail Transit Facilities-Part 1:General. State Administration for Market Regulation. National Standardization Administration: Beijing, China, 2020; p. 12.
18. Zhang, X.; Ding, Y.; Zhao, H.; Yi, L.; Guo, T.; Li, A.; Zou, Y. Mixed Skewness Probability Modeling and Extreme Value Predicting for Physical System Input–Output Based on Full Bayesian Generalized Maximum-Likelihood Estimation. *IEEE Trans. Instrum. Meas.* **2024**, *73*, 2504516. [CrossRef]
19. Zhao, H.; Zhang, X.; Ding, Y.; Guo, T.; Li, A.; Soh, C.K. Probabilistic mixture model driven interpretable modeling, clustering, and predicting for physical system data. *Eng. Appl. Artif. Intell.* **2025**, *160*, 112069. [CrossRef]